ACS OMEGA

http://pubs.acs.org/journal/acsodf

Article

Interfacial Delamination at Multilayer Thin Films in Semiconductor Devices

Jin-Hoon Kim,[‖] Hye-Jun Kil,[‖] Sangjun Lee, Jinwoo Park, and Jin-Woo Park*

Cite This: *ACS Omega* 2022, 7, 25219−25228

Read Online

ACCESS | Metrics & More | Article Recommendations | Supporting Information

ABSTRACT: With the evolution of semiconducting industries, thermomechanical failure induced in a multilayered structure with a high aspect ratio during manufacturing and operation has become one of the critical reliability issues. In this work, the effect of thermomechanical stress on the failure of multilayered thin films on Si substrates was studied using analytical calculations and various thermomechanical tests. The residual stress induced during material processing was calculated based on plate bending theory. The calculations enabled the prediction of the weakest region of failure in the thin films. To verify our prediction, additional thermomechanical stress was applied to induce cracking and interfacial delamination by various tests. We assumed that, when accumulated thermomechanical-residual and externally applied mechanical stress becomes larger than a critical value the thin-film cracking or interfacial delamination will occur. The test results agreed well with the prediction based on the analytical calculation in that the film with maximum tensile residual stress is the most vulnerable to failure. These results will provide useful analytical and experimental prediction tools for the failure of multilayered thin films in the device design stage.

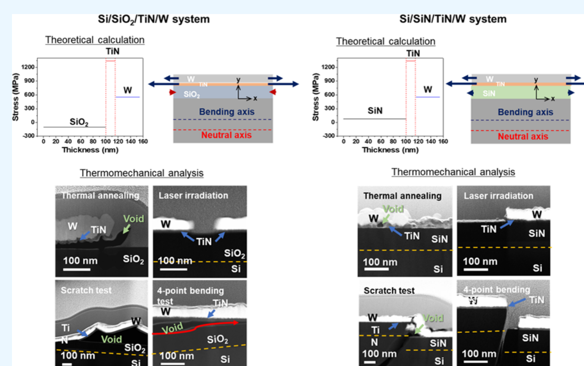

1. INTRODUCTION

Since the invention of field-effect transistors in the 1920s, one of the main issues in the semiconductor industry has been the fabrication of faster and smaller transistors.[1] Currently, for highly integrated devices, the channel width of the device has decreased to less than 10 nm.[2,3] However, the processing technology is limited in terms of further decreasing the channel width.[2,4] Hence, semiconductor devices with multilayered structures have evolved to increase the degree of integration.[4,5] Such multilayered devices have the advantages of high density, low cost, and low power consumption.[3]

For multilayered semiconductor devices, various nanostructures with high aspect ratios, such as nanoplates, nanopillars, and nanowires, should be fabricated.[6] Among the various nanostructures, nanoplates with oxide or nitride/nitride/metal multilayers are one of the essential components in thin-film transistors since oxide, nitride, and metal layers are used as the gate dielectric, adhesion layer, and gate metal in metal/insulator/semiconductor (MIS) structures, respectively.[4] For smaller channel widths and higher stacks, the thickness of the thin films should be decreased,[7] which makes the thin films more vulnerable to various thermomechanical failures, such as bending, cracking, and, particularly, interfacial delamination.[8,9] These factors eventually lead to the catastrophic failure of the devices.[4]

As stated previously, the interfacial delamination between thin films has become the most critical device failure mode because more complex residual stresses are induced by increasing the number of layers in the multilayered films during deposition processes and operations. Heat release during device operation has increased with the number of layers in the multilayered films due to thermal cycling.[10−13] Upon the cyclic heating and cooling during the deposition process and operation of the devices,[4] thermomechanical-residual stress is induced in the films and substrates due to mismatches in the coefficient of thermal expansion (CTE), Young's modulus, and Poisson's ratio of the constituent film materials and the substrate, which is the well-known cause of failure in thin-film devices.[14]

Simple analytical calculation methods for the residual stresses in the single film deposited on a thick substrate, which can be readily used in industries, have been well developed and can be readily used in industries.[15,16] Hence, the prediction of the weakest region to undergo thermomechanical failure can be readily made if the thermomechanical processing conditions and material properties are known.[17] However, the above-mentioned simple prediction process cannot be applied to the multilayer thin films, and the

Received: April 6, 2022
Accepted: June 29, 2022
Published: July 14, 2022

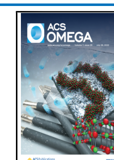

© 2022 The Authors. Published by American Chemical Society

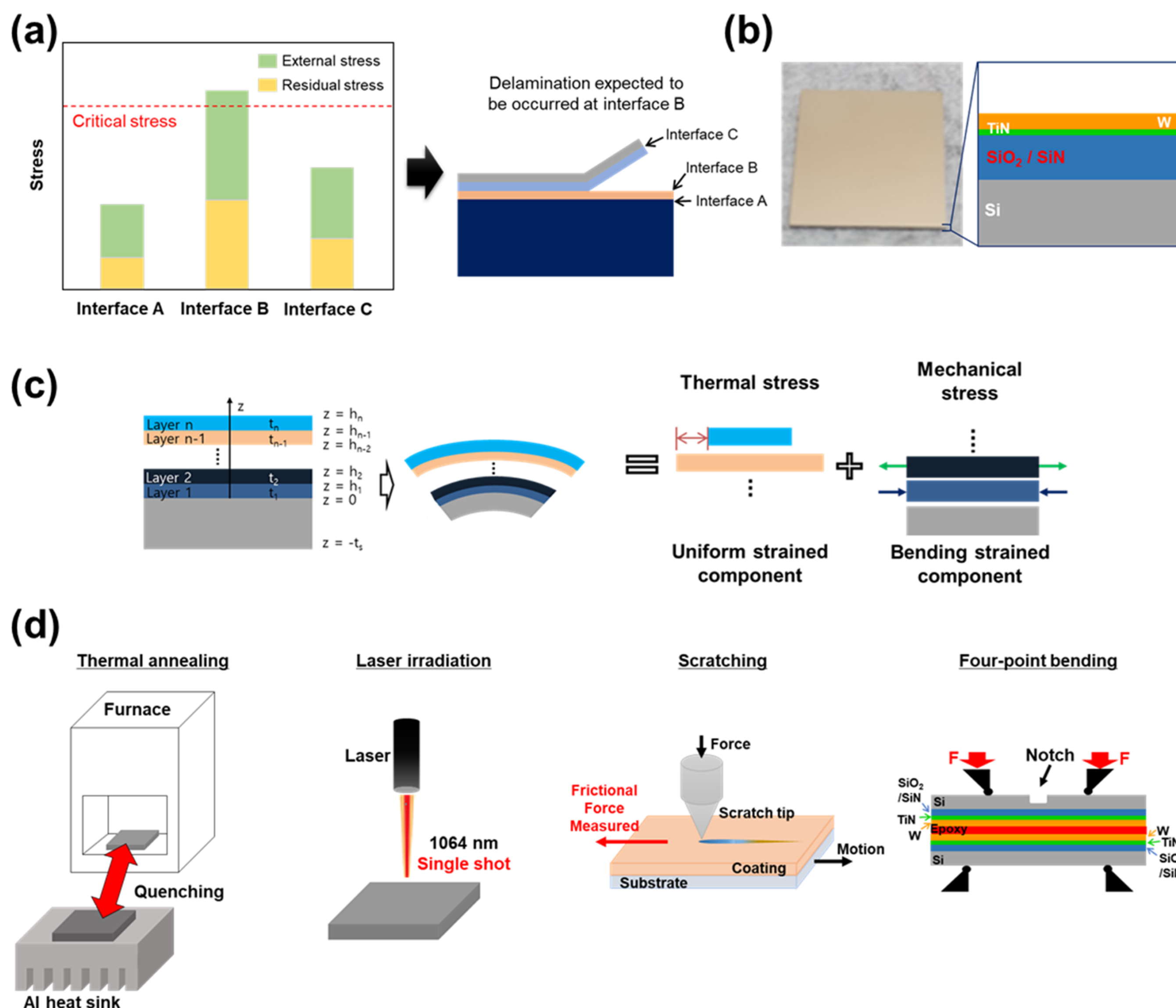

Figure 1. (a) Schematic description that thin-film failure occurs beyond a critical stress. (b) Real specimen image and the multilayered structure. "Photograph courtesy of "Hye-Jun Kil." Copyright 2022." (c) Schematic descriptions of strain components in the multilayer system after heating or cooling. (d) Schematic descriptions of the thermomechanical tests performed in this study.

experimental verification process should be carefully designed accordingly.[4,18] Also, comprehensive analytical and experimental methods that could consider the effect of CTE and Young's modulus mismatch in the multilayered system are required.[19] However, current methods that use analytical tools such as finite element modeling to predict fracture behavior by thermal stress used mechanical experiments such as four-point bending tests to verify their prediction.[20,21] The main parameter affecting fracture behavior in these mechanical analyses was mechanical properties such as Young's modulus and Poisson's ratio. Hence, it was unsuitable for thermomechanical analysis in which the CTE mismatch also should be considered.

In this work, the residual stress distribution throughout the multilayer thin films and the substrate induced due to the temperature changes during the deposition was modeled analytically based on plate bending theory.[18,22] Plate bending theory has been widely used to model the residual stress distribution in multilayered structures.[23,24] The detailed structures and material properties of two multilayer specimens are summarized in Figure 1 and Tables 1 and 2.

Table 1. Descriptions of Specimens A and B

	Si	SiO_2	SiN	TiN	W
specimen A	770 μm	100 nm		15 nm	40 nm
specimen B	770 μm		100 nm	15 nm	40 nm

Table 2. Properties of the Materials Used in This Work

materials	α (10^{-6}/K)	E (GPa)
Si	2.6[25]	130[25]
SiO_2	0.7[26]	70[27]
SiN	3.27[28]	149[29]
TiN	9.4[30]	250[31]
W	4.3[32]	410[33]

https://doi.org/10.1021/acsomega.2c02122
ACS Omega 2022, 7, 25219−25228

We focused on the external stresses such as significant temperature change during the operation as the main reason for the device failure, because the device did not show any failure after the deposition process. Hence, we assumed that the residual stresses during deposition processes were much lower than the critical stress for the device failure, as schematically shown in Figure 1a. The multilayered structures were deposited based on optimized processes to minimize defects, and residual stress occurred during fabrication processes.

The experimental investigation of the failure modes was simultaneously performed by four different thermomechanical test methods, including thermal annealing, laser irradiation, scratch test, and four-point bending test. Especially, the four-point bending test has been frequently used for calculating interfacial fracture energy in various thin-film structures.[21] To identify the location of delamination, analyses by field-emission scanning electron microscopy (FE-SEM) and transmission electron microscopy (TEM) were performed. The experimental results clearly verified that the tensile residual stresses induced at the film are the primary factor for the interfacial delamination and cracking.

2. ANALYTICAL CALCULATION AND EXPERIMENTAL PROCEDURES

All of the experiments were carried out using multilayered specimens with thin films deposited in the order of 100 nm silicon oxide (SiO_2) or silicon nitride (SiN), 15 nm titanium nitride (TiN), and 40 nm tungsten (W) on a 770 μm thick silicon (Si) wafer. A schematic description of the samples is shown in Figure 1a,b and Table 1. First, 100 nm SiO_2 or SiN was deposited on a Si wafer using chemical vapor deposition (CVD), then, 15 nm TiN was deposited using atomic layer deposition (ALD), and finally, 40 nm W was deposited using CVD. The largest temperature change (ΔT) during deposition processes is 490 °C.

The residual stress distribution in the multilayers during the deposition process was calculated using plate bending theory.[18,22] The distribution of thermomechanical-residual stress within the multilayered thin films was theoretically predictable through the following calculations. Strain due to heating and cooling of a multilayer system with n thin film is[22]

$$\varepsilon = c + \frac{z - t_b}{r} \quad (-t_s \le z \le h_n) \tag{1}$$

where c is the uniform strain component, z is the bending axis, t_b is the bending strain component, $1/r$ is the curvature of the sample, t_s is the thickness of the Si wafer, and h_n is the thickness of the entire n films. Stress distribution on the Si wafer substrate is calculated as[22]

$$\sigma_s = E_s(\varepsilon - \alpha_s \Delta T) \quad (-t_s \le z \le 0) \tag{2}$$

where E_s is Young's modulus of the Si wafer, α_s is the CTE of the Si wafer, and ΔT is the temperature difference during heating or cooling. Stress distribution on each thin film (ith from the interface with the substrate) can be expressed as[22]

$$\sigma_i = E_i(\varepsilon - \alpha_i \Delta T) \quad (i = 1 \text{ to } n) \tag{3}$$

where E_i is Young's modulus and α_i is the CTE of the ith thin film. Based on the above equation, a general solution can be obtained. The uniform strain component (eq 5) and bending strain component (eq 7) can be obtained from the force balance equation (eq 6), and the curvature (eq 9) can be obtained from the momentum balance equation (eq 8).[22]

$$E_s(c - \alpha_s \Delta T)t_s + \sum_{i=1}^{n} E_i(\varepsilon - \alpha_i \Delta T)t_i = 0 \tag{4}$$

$$c = \frac{(E_s t_s \alpha_s + \sum_{i=1}^{n} E_i t_i \alpha_i)\Delta T}{E_s t_s + \sum_{i=1}^{n} E_i t_i} \tag{5}$$

$$\int_{-t_s}^{0} \frac{E_s(z - t_b)}{r}\,dz + \sum_{i=1}^{n} \int_{h_{i-1}}^{h_i} \frac{E_i(z - t_b)}{r}\,dz = 0 \tag{6}$$

$$t_b = \frac{-E_s {t_s}^2 + \sum_{i=1}^{n} E_i t_i(2h_{i-1} + t_i)}{2(E_s t_s + \sum_{i=1}^{n} E_i t_i)} \tag{7}$$

$$\int_{-t_s}^{0} \sigma_s(z - t_b)\,dz + \sum_{i=1}^{n} \int_{h_{i-1}}^{h_i} \sigma_i(z - t_b)\,dz = 0 \tag{8}$$

$$\frac{1}{r} = \left\{3\left[E_s(c - \alpha_s \Delta T){t_s}^2 - \sum_{i=1}^{n} E_i t_i(c - \alpha_i \Delta T)(2h_{i-1} + t_i)\right]\right\} \Big/ \left\{E_s {t_s}^2(2t_s + 3t_b) + \sum_{i=1}^{n} E_i t_i[6{h_{i-1}}^2 + 6h_{i-1}t_i + 2{t_i}^2 - 3t_b(2h_{i-1} + t_i)]\right\} \tag{9}$$

Since t_s is much thicker than the thickness of the thin film, the first-order approximation can be applied,[22] and eqs 5, 7, and 9 are simplified as eqs 10−12, respectively. Finally, σ_s and σ_i can be calculated as in eqs 13 and 14, respectively

$$c = \alpha_s \Delta T + \sum_{i=1}^{n} \frac{E_i t_i(\alpha_i - \alpha_s)\Delta T}{E_s t_s} \tag{10}$$

$$t_b = -\frac{t_s}{2}\left[1 - \sum_{i=1}^{n} \frac{E_i t_i}{E_s t_s}\right] \tag{11}$$

$$\frac{1}{r} = 6\sum_{i=1}^{n} \frac{E_i t_i(\alpha_i - \alpha_s)\Delta T}{E_s {t_s}^2} = \sum_{i=1}^{n} \frac{1}{r_i} \tag{12}$$

$$\sigma_s = \frac{2}{{t_s}^2}\left(3z + 2t_s - \frac{2}{E_s}\sum_{j=1}^{n} E_j t_j\right)\sum_{i=1}^{n} E_i t_i(\alpha_i - \alpha_s)\Delta T \quad (-t_s \le z \le 0) \tag{13}$$

where t_s, t_j, t_i, E_s, E_j, E_i, α_s, α_i, and ΔT are the thicknesses of the Si substrate, the jth thin film, and the ith thin film; Young's modulus values of the Si substrate, the ith thin film, and the jth thin film; CTE of the Si substrate and the ith thin film; and the temperature change during post thermal annealing, respectively.

$$\sigma_i = E_i\left[\alpha_s - \alpha_i + 4\sum_{j=1}^{n} \frac{E_j t_j(\alpha_j - \alpha_s)}{E_s t_s}\right]\Delta T \tag{14}$$

To verify our calculation result based on eq 14, we applied the well-known assumption that there is a critical stress over which a material fails.[34] If the critical stress is known, and we can measure the external stress initiating the failure, the

https://doi.org/10.1021/acsomega.2c02122
ACS Omega 2022, 7, 25219−25228

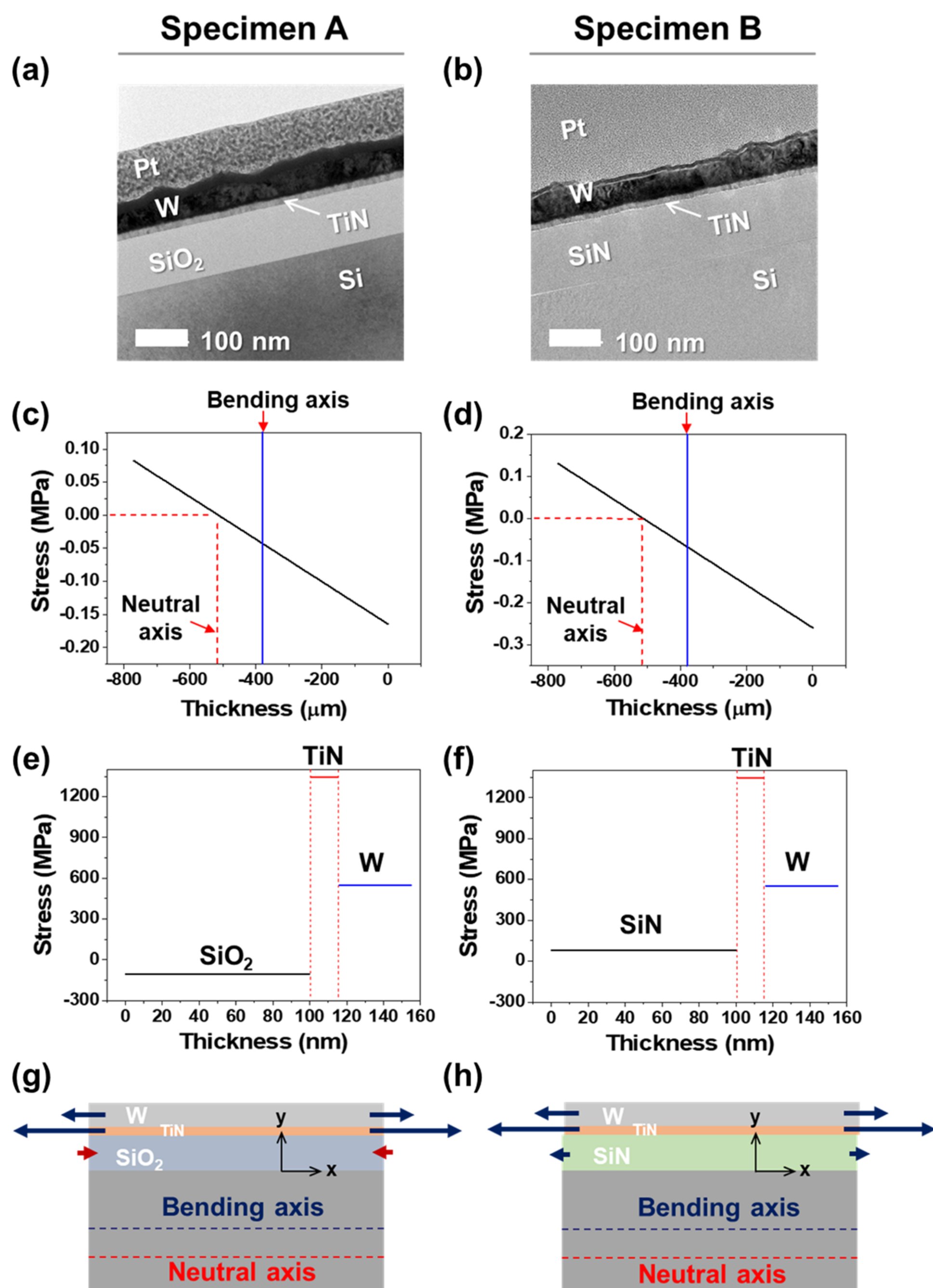

Figure 2. Cross sectional TEM images of (a) SiO_2- and (b) SiN-based multilayered systems. Stress distribution in the Si substrate of the (c) Specimen A and (d) Specimen B. Stress distributions in the deposited thin films of (e) Specimen A and (f) Specimen B. Schematic stress distributions of (g) Specimen A and (h) Specimen B after cooling. A Pt layer shown in Figure 2a,b was deposited for TEM analysis, which is irrelevant to the multilayered systems.

residual stress can be calculated (Figure 1a). Herein, we focused on the situation in which failure occurs as the device without failure operates. That is, the residual stress is a level that does not reach the critical stress, and a value equal to or higher than the threshold stress is applied by the external stress generated while the device is operating, thus causing failure. A specimen having a very low defect density through an optimized manufacturing process could be used to implement a state in which there was no failure before operating.

In this study, external stress was imposed on the samples by four different methods: thermal annealing and quenching, laser irradiation, scratching, and four-point bending tests. For the thermal annealing and quenching test, the specimens in Table 1 were put into a thermal furnace at 800 °C for 75 s. Since the annealing time was quite long, we could ignore the thermal diffusion throughout the specimen. Then, the annealed samples were quenched to room temperature using an aluminum heat sink. As ΔT in the thermal test is larger than that of the deposition process (490 °C), greater residual stresses than those during the deposition were induced in the thin films.

For laser irradiation tests, a pulsed ND:YAG laser with a wavelength of 1064 nm and a pulsed width of 6 ns was used. For irradiation, one shot of the laser beam was irradiated on

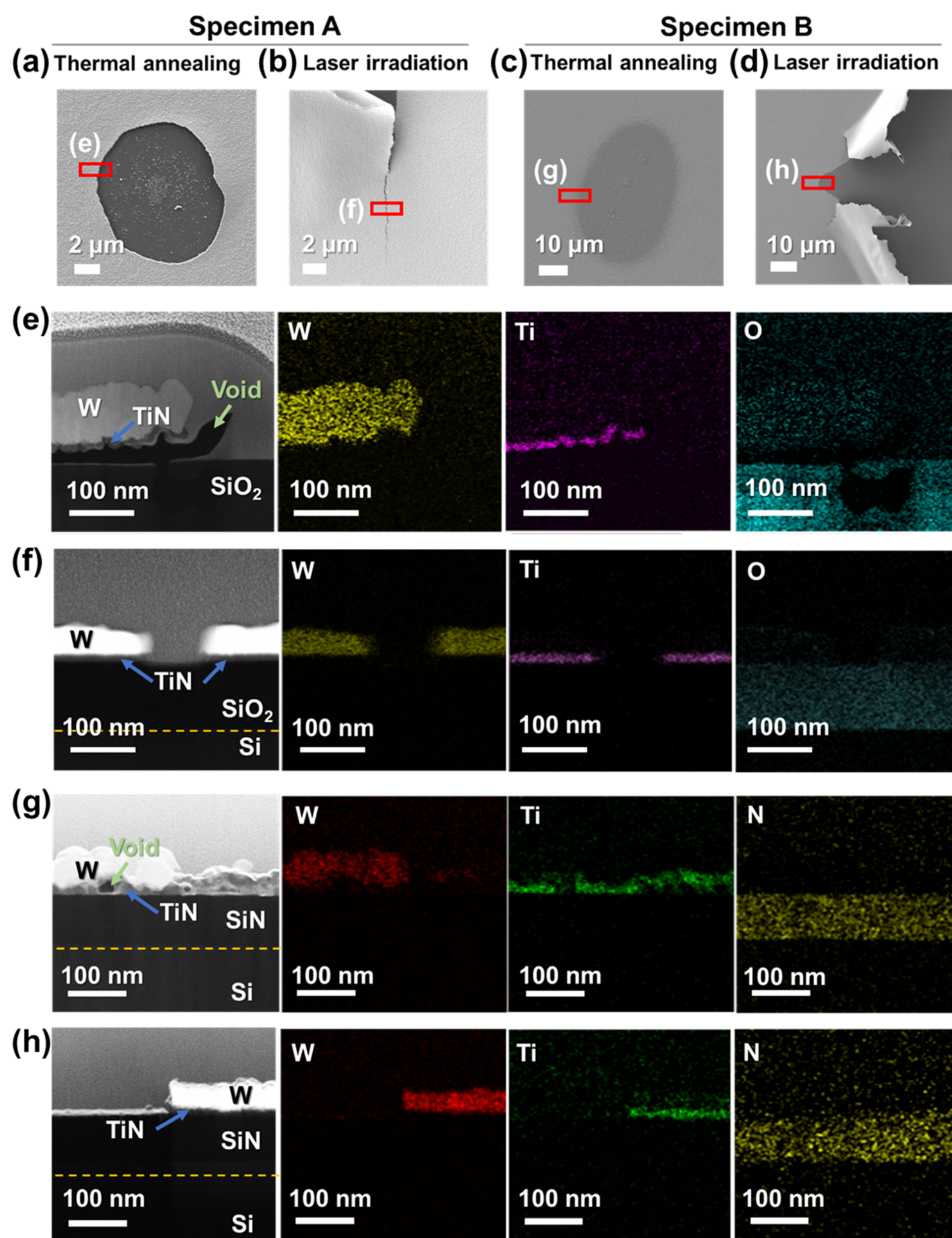

Figure 3. Field-emission scanning electron microscopy (FE-SEM) images of the delaminated surfaces of (a), (b) Si/SiO_2/TiN/W and (c), (d) Si/SiN/TiN/W induced by thermal annealing ((a) and (c)) and laser irradiation ((b) and (d)). The red rectangular area in Figure 3a−d is the location where cross sectional sampling for TEM was performed using FIB. Cross sectional TEM and EDS mapping images of the (e) Si/SiO_2/TiN/W system and (g) Si/SiN/TiN/W system after thermal annealing and quenching. Cross sectional TEM and EDS mapping images of the (f) Si/SiO_2/TiN/W system and (h) Si/SiN/TiN/W system after laser irradiation.

the specimen surface. By the irradiation, ΔT is expected to be around 9500 °C.[35] The heating and cooling cycle will be significantly shorter than the thermal test. Since the pulse duration of the laser was relatively long, and the thickness of each layer was less than 100 nm, we could assume that the absorption length of the laser energy in the multilayered structure was smaller than the thickness of each layer. Hence, thermal diffusion was not considered in the laser irradiation analysis.[36,37] During the laser irradiation, external stresses due to significant temperature change overcome the critical stress, resulting in the failure of the multilayered structures.

A scratch test was conducted in accordance with ISO 20502 and ASTM C1624.[38] A nanoscale scratch tester (CSM, USA) with a sharp diamond tip was used. The diamond tip is 2 μm in radius. The vertical load at the start is 0.5 mN, and the end force is 120 mN. During the scratch test, the diamond tip scratches the surface of the specimen with a constant increase in the vertical load at a rate of 2 mN/s. Hence, the adhesion force of the thin film could be verified by measuring the vertical loads where delamination occurs.

For the four-point bending test, specimens were cut into 50 mm by 8 mm rectangles using a laser dicing machine. Two specimens were bonded together using an epoxy, with the thin films facing each other (Figure 1d). Additionally, in one of the bonded specimens, a notch was formed on the opposite side of the deposited thin films using a dicing saw. The four-point bending test was performed using a universal testing machine (CT-UTM101E, CoreTech, Korea). The displacement veloc-

https://doi.org/10.1021/acsomega.2c02122
ACS Omega 2022, 7, 25219−25228

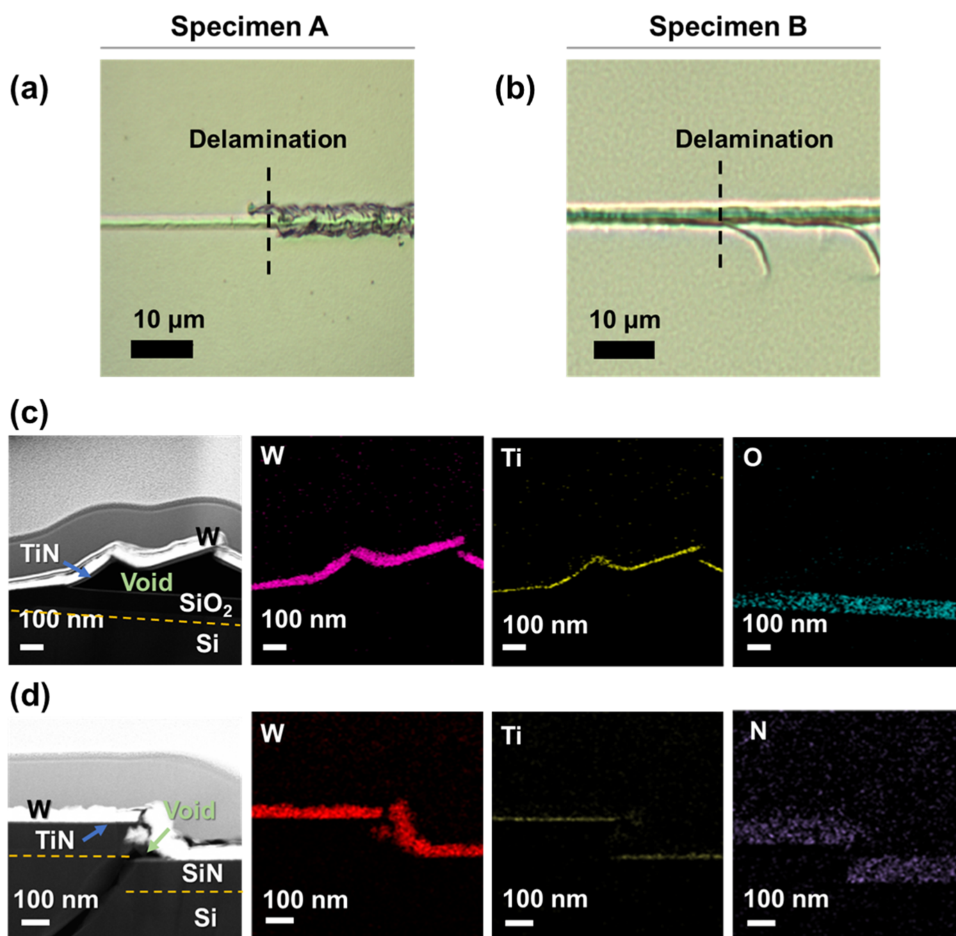

Figure 4. OM surface images of the (a) Specimen A and (b) specimen B after the scratch test. Cross sectional TEM and EDS mapping images of the (c) Specimen A and (d) Specimen B after scratch tests.

ity was 10 mm/min, and the inner pin and outer pin distances were 20 and 45 mm, respectively (Figure 1d). During the four-point bending test, tensile stress was applied to the specimen. The crack initiated at the notch propagated through the layers. When the crack reached the interface with weak interfacial adhesion strength, the crack would propagate through the interface. Otherwise, the crack would propagate throughout the layers further, which would result in surface crack propagation.[21] Hence, in the four-point bending test, the interfacial adhesion strength is critical for determining the crack propagation path.

The cross sections of the failed specimens were analyzed using FE-SEM (JSM-6701F, JEOL, Japan), and the crack location and site of delamination were identified. The delaminated or cracked area was milled using a focused ion beam (FIB, crossbeam 540, ZEISS, Germany), and, using TEM (JEM-F200, JEOL, Japan), materials were identified with energy-dispersive X-ray spectroscopy (EDS) mapping.

3. RESULTS AND DISCUSSION

3.1. Calculation of the Residual Thermal Stress Based on Plate Bending Theory.

The cross sectional TEM images of Specimen A and B are shown in Figure 2a,b. TiN was deposited between SiO_2 or SiN and W to improve adhesion. As shown in Figure 2a,b, defects and blisters were not observed after deposition. The properties of the materials used in this work are summarized in Table 2. To calculate the residual stress induced in the multilayered systems during the deposition process, plate bending theory was used, as described in detail in Section 2.[18,22] Based on plate bending theory, the residual stress induced in the Si substrate (σ_s) with n thin films is expressed in eq 13. The thermal residual stress induced in the ith thin film from the interface with the Si substrate is expressed in eq 14.

In Specimens A and B in Figure 2a,b, the thermomechanical-residual stresses were calculated using eqs 13 and 14, and the results are plotted in Figure 2c−f. As shown in Figure 2c,d, a neutral plane is located at 513 μm from the surface of the Si substrate both in Specimens A and B, which is approximately 2/3 of the total thickness of the Si substrate.

As shown in Figure 2e,f, the residual stresses in the thin films are much higher than those in the Si substrates. In the thin films, the sign of the stress is determined by the CTE mismatches between the Si substrate and the thin films. CTE of SiO_2 is lower than that of the Si substrate; hence, compressive stress is generated in the SiO_2 layer (Table 2). On the other hand, tensile stress is induced in the SiN, TiN, and W layers since their CTEs are higher than that of the Si substrate (Table 2). According to the stress distribution in the thin films shown in Figure 2e,f, the strain mismatch is largest at the interfaces between SiO_2 and TiN and between SiN and TiN for Specimen A and B, respectively. Based on the stress distributions, TiN where the largest tensile stress is induced and for which the stiffness is the lowest due to the smallest

thickness seems to be the most vulnerable layer to cracking and delamination.

3.2. Thermal Annealing and Laser Irradiation. To verify the prediction made in Section 3.1, additional thermomechanical stresses were applied by thermal annealing and laser irradiation. First, samples were thermally annealed at 800 °C and quenched to room temperature. This ΔT is larger by 375 °C than that induced during deposition. An Al heat sink was used to quench the heated samples, and an IR camera was used to confirm that the temperature was immediately reduced to room temperature. As shown in the FE-SEM images in Figure 3a,c, a delaminated area was observed on the multilayered samples. According to the cross sectional TEM images and EDS mapping results in Figure 3e,g, TiN layers were delaminated or cracked under the thermomechanical stresses in both Specimens A and B, respectively. This agrees very well with the theoretical prediction made in Section 3.1. The void formation shown in Figure 3g is that quenching was performed in the atmosphere after thermal annealing. The difference between Young's modulus and Poisson's ratio causes thermal expansion mismatch between layers, resulting in delamination. At this point, microcracks occurred, and voids were created between TiN and SiN.[39]

In the laser irradiation test (Figure 1d), the laser heat was focused on a small area of specimen surfaces for a very short time, and the specimens were cooled in air.[40] First, the critical pulse energy for delamination was investigated by observing the irradiated surface using an optical microscope (OM). As shown in Figure S1 (Supporting Information), when the pulse energies were 57 and 90 mJ, delamination and cracking occurred on the surfaces of Specimens A and B, respectively. When the laser power was higher than this critical power, the total delaminated area increased, as shown in Figure S1. The detailed delaminated surface at the critical laser power is shown in Figure 3b,d. The main reason for the delamination or cracking of the specimens' surface by this laser irradiation is the difference between Young's modulus and Poisson's ratio between the multilayers. The difference between the two values causes a difference in the degree of expansion of the layers, and it causes the occurrence of strain by this mismatch, occurring delamination. Based on the cross sectional images shown in Figure 3f,h, delamination occurred at the interfaces between SiO_2 and TiN and between SiN and TiN, respectively, which corresponds very well with the thermal annealing tests as well as the calculation result in Section 3.1.

3.3. Nanoscratch and Four-Point Bending Tests. Additional mechanical stresses were imposed on the two specimens by nanoscratch and four-point bending tests to verify the relationship between the residual stresses and the thin-film failure. The mean critical forces of the tangential force at which delamination occurred were measured as 7 mN for Specimen A and 15 mN for Specimen B. As in the laser irradiation test, a larger energy was required to delaminate Specimen B than Specimen A. Also, the delaminated films by the nanoscratch test were TiN as in the thermal annealing and laser irradiation tests. The interfacial delamination at SiO_2/TiN in Specimen A and SiN/TiN interfaces in Specimen B was confirmed by OM, TEM images, and EDS mapping, as shown in Figure 4.

Finally, the four-point bending test was performed to further verify the layer that is most vulnerable to failure in the multilayered systems. A notch was formed at the bottom of the Si wafer, as shown in Figure 5a, and two samples were bonded

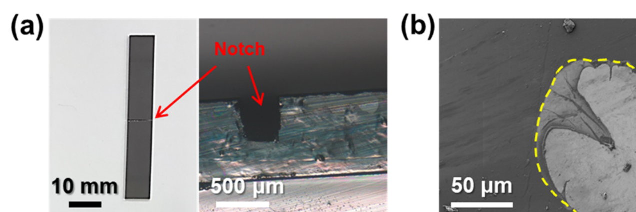

Figure 5. (a) OM image of the notch induced on the opposite surface of the thin-film-deposited Si wafer. "Photograph courtesy of "Jin-Hoon Kim." Copyright 2022." (b) FE-SEM image of the Si/SiN/TiN/W system after the four-point bending test. The yellow dotted line represents the point where the cohesive failure of the epoxy occurred.

using epoxy as in Figure 1d. When the mechanical bending was induced, a crack was generated at the notch, and it was propagated to the bonded interfaces. Then, the crack propagated along the interface or through the layer if the summation of the mechanical stress and the residual stress becomes larger than a critical value for failure.[17]

First, the cross sections of the delaminated surface after the four-point bending test were analyzed. As shown in Figure 6a,c, delamination occurred at the interface between SiO_2 and TiN in Specimen A, which matches well with the previous test and calculation results in Sections 2 and 3, respectively. In Specimen B, interfacial delamination was observed at the interface between SiN and TiN, and the interfacial crack detoured through the W layer rapidly. As shown in Figure 6a, the branching of cracks was not observed in specimen A because cracks propagated through the weak SiO_2/TiN interface, as shown in Figure 6c. Whereas, as shown in Figure 6b, branching of cracks was observed on the surface of Specimen B because propagated cracks detoured through the W layer.

Based on fracture mechanics, if the interfacial strength was stronger than the intrinsic material's strength, the crack propagated through the thin film in the vertical direction. Whereas when the interfacial strength was weaker than the intrinsic material's strength, the crack propagated through the weak interface in the lateral direction.[41] Crack branching occurred due to rapid rupture of the brittle materials. In specimen B, since the crack propagated through films (vertical direction to the specimen), the crack rapidly reached the surface. Hence, the branching was observed, as shown in Figure 6b. Whereas in specimen A, since the crack propagated through the interface (lateral direction), it took longer for cracks to reach the surface. Hence, we could not observe the branching in specimen A, as shown in Figure 6a. Also, as shown in Figure 6e, we could observe a plateau in the stress−displacement curve, which indicates slow crack propagation through the interface. Such differences in crack propagation behavior observed after four-point bending tests strongly indicate that the SiN/TiN interface has stronger adhesion strength compared with SiO_2/TiN, also shown in the analytical calculation, laser irradiation, and scratch tests.

The interfacial fracture energy, which is the critical strain energy release rate (G), can be calculated from the force−displacement curve obtained from the four-point bending test, which is expressed as[42]

$$G = \frac{21(1-\nu^2)M^2}{4Eh^3} \tag{15}$$

https://doi.org/10.1021/acsomega.2c02122
ACS Omega 2022, 7, 25219−25228

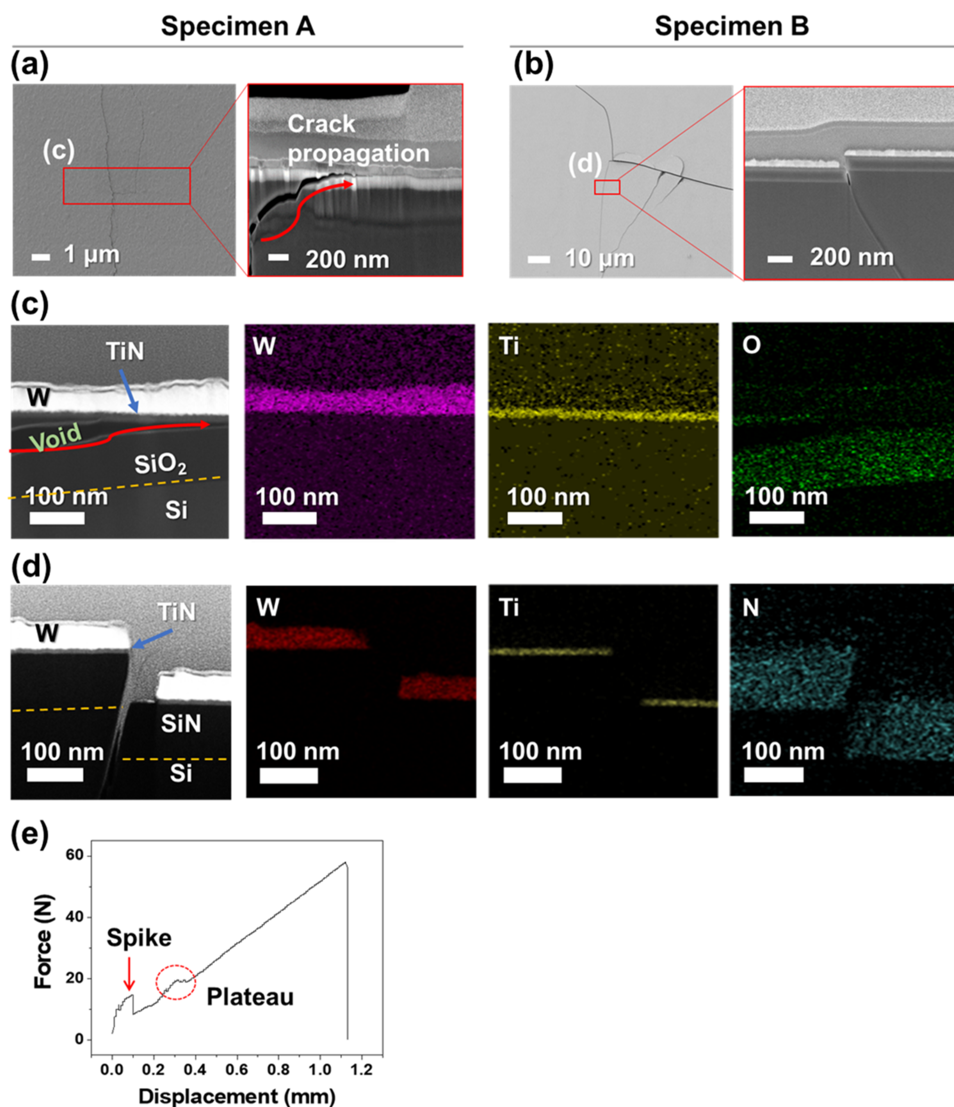

Figure 6. Surface and cross sectional FE-SEM images of the (a) Si/SiO_2/TiN/W system and (b) Si/SiN/TiN/W system after the four-point bending test. Cross sectional TEM and EDS mapping images of the (c) Si/SiO_2/TiN/W system and (d) Si/SiN/TiN/W system after the four-point bending test, respectively. (e) Force−displacement curves of the Si/SiO_2/TiN/W system obtained during the four-point bending test.

where M is the bending moment, which can be expressed as $M = PL/2b$ in the plate beam; P is the bending load; L is the spacing between loading pins; b is the width of the specimen; ν is Poisson's ratio of the Si substrate; E is Young's modulus of the Si substrate; and h is the thickness of the specimen.

The force−displacement curve obtained from the four-point bending test is shown in Figure 6e, revealing that the force was linearly increased first, which is the overall deformation of the specimen. Then, a crack was formed at the notch and propagated through the bonded interface. The crack at the notch led to the formation of a spike in the force−displacement curve, as shown in Figure 6e. After the spike was formed, the load was relaxed and then showed linear-elastic behavior. When the displacement increased further, a plateau was formed, where delamination started. The force value at the plateau was used to calculate G using eq 15, and the calculated G value was 19 J/m^2 in Specimen A, which is comparable to the reported G values of thin films deposited on the Si substrate.[43−45] After the crack was formed at the notch, the bending of the specimen mostly occurred to the un-notched side of the specimen (schematically shown in Figure 1d), which is independent of the notch's depth. Hence, in the four-point bending test, the effect of notch depth is known to be negligible.[46]

Kim et al. measured the G of a photosensitive dielectric/Ti/Cu multilayered system deposited on a Si wafer using the four-point bending test, and they reported that interfacial delamination occurred at the photosensitive dielectric/Ti interface; the G value was approximately 17.3 J/m^2.[43] Völker et al. measured the G value of a borophosphosilicate dielectric glass (BPSG)/Ti/W/AlSiCu multilayered system on a Si wafer using the four-point bending test.[44] They also reported that delamination occurred at the BPSG/Ti interface, and the G value was approximately 11.7 J/m^2.[44] Ma et al. analyzed the adhesion property of a Si/SiO_2/AlCu/TiN/SiO_2 multilayered system on a Si wafer using the four-point bending test. They also reported that delamination occurred at the SiO_2/TiN interface, but the interfacial fracture energy was not measured.[45]

https://doi.org/10.1021/acsomega.2c02122
ACS Omega 2022, 7, 25219−25228

4. CONCLUSIONS

In this study, the film failure that occurred in oxide/nitride/metal or nitride/nitride/metal multilayer systems for semiconductor devices was analyzed theoretically and experimentally. Based on plate bending theory, the largest tensile residual stress was predicted to be induced at the TiN layer in two different specimens, which makes the TiN layer and its interfaces with TiN most vulnerable to cracking and delamination, respectively. To verify the theoretical prediction, thermal annealing and laser irradiation tests were performed to induce additional thermomechanical stresses. In addition, external mechanical stress was also induced using the scratch test and four-point bending test. The four test results all agreed well with the theoretical prediction that the TiN layer and the interfaces with it are the weakest region to failure. These agreements clearly confirm that the region of failure in multilayered thin films can be predicted based on the residual stresses that are calculated analytically. In conclusion, the analytical model and experimental test methods proposed in this work will be useful tools to evaluate the mechanical stability of a designed multilayer thin-film system on Si before fabrication and during operation.

■ ASSOCIATED CONTENT

Supporting Information

The Supporting Information is available free of charge at https://pubs.acs.org/doi/10.1021/acsomega.2c02122.

Photographs and optical microscope (OM) images of (a) specimen A and (b) specimen B with different laser irradiation power (PDF)

■ AUTHOR INFORMATION

Corresponding Author

Jin-Woo Park − *Department of Materials Science and Engineering, Yonsei University, Seoul 03722, Korea;* orcid.org/0000-0003-0965-373X; Email: jwpark09@yonsei.ac.kr

Authors

Jin-Hoon Kim − *Media Lab, Massachusetts Institute of Technology, Cambridge, Massachusetts 02139, United States*
Hye-Jun Kil − *Department of Materials Science and Engineering, Yonsei University, Seoul 03722, Korea*
Sangjun Lee − *Department of Materials Science and Engineering, Yonsei University, Seoul 03722, Korea*
Jinwoo Park − *Computational Science Engineering Team, Samsung Electronics Co., Ltd., Hwaseong 18448, Korea*

Complete contact information is available at:
https://pubs.acs.org/10.1021/acsomega.2c02122

Author Contributions

‖J.-H.K. and H.-J.K. contributed equally to this work.

Notes

The authors declare no competing financial interest.

■ ACKNOWLEDGMENTS

This research was supported by the Joint Program for Samsung Electronics-Yonsei University.

■ REFERENCES

(1) Lee, S.-H. Technology Scaling Challenges and Opportunities of Memory Devices. In *2016 IEEE International Electron Devices Meeting (IEDM)*, December 3−7, 2016; pp 1−8.
(2) Yu, B.; Chang, L.; Ahmed, S.; Wang, H.; Bell, S.; Yang, C.-Y.; Tabery, C.; Ho, C.; Xiang, Q.; King, T.-J.; et al. FinFET Scaling to 10 nm Gate Length. In *Technical Digest, International Electron Devices Meeting*, San Francisco, CA, December 8−11, 2002; pp 251−254.
(3) Lee, S. K.; Ma, S.-M.; Seo, I.-S.; Shin, H. S.; Kim, H.; Cross, A.; Baris, O.; Kim, D.; Lee, S. H.; Lange, S. Investigation of Novel Inspection Capability for 3D NAND device wordline inspection. In *25th Annual SEMI Advanced Semiconductor Manufacturing Conference (ASMC 2014)*, May 19−21, 2014; pp 278−282.
(4) Namkoong, Y.; Yang, H. J.; Song, Y. H. Mechanical Stress Distribution and the Effects of Process Parameter Changes in Vertical NAND Flash Memory. *J. Nanosci. Nanotechnol.* **2017**, *17*, 5055−5060.
(5) Nowak, E.; Kim, J.; Kwon, H.; Kim, Y.; Sim, J. S.; Lim, S.; Kim, D. S.; Lee, K.; Park, Y.; Choi, J.; Chung, C. Intrinsic Fluctuations in Vertical NAND Flash Memories. In *Symposium on VLSI Technology (VLSIT)*, June 12−14, 2012; pp 21−22.
(6) Joodaki, M. Uprising nano memories: Latest advances in monolithic three dimensional (3D) integrated Flash memories. *Microelectron. Eng.* **2016**, *164*, 75−87.
(7) Lung, C.-Y.; Chung, Y.; Wu, M.; Lee, H.; Lian, N.; Yang, T.; Chen, K.; Lu, C. Pre-Epitaxial Plasma Etch Treatment for the Selective Epitaxial Growth of Silicon in High Aspect Ratio 3D NAND Memory. In *30th Annual SEMI Advanced Semiconductor Manufacturing Conference (ASMC)*, May 6−9, 2019; pp 1−5.
(8) Zhang, S. M.; Kuo, Y. Temperature Effect on Dielectric Breakdown and Charges Retention of Nanocrystalline Cadmium Selenide Embedded Zr-Doped HfO_2 High-k Dielectric Thin Film. *IEEE Trans. Device Mater. Reliab.* **2016**, *16*, 561−569.
(9) Chiu, C. C.; Huang, C. J.; Yang, S. Y.; Lee, C. C.; Chiang, K. N. Investigation of the delamination mechanism of the thin film dielectric structure in flip chip packages. *Microelectron. Eng.* **2010**, *87*, 496−500.
(10) Sebastiani, M.; Rossi, E.; Zeeshan Mughal, M.; Benedetto, A.; Jacquet, P.; Salvati, E.; Korsunsky, A. M. Nano-Scale Residual Stress Profiling in Thin Multilayer Films with Non-Equibiaxial Stress State. *Nanomaterials* **2020**, *10*, 853.
(11) Liu, S.; Lia, Y.; Chena, P.; Lia, W.; Gaoa, S.; Zhang, B.; Yeb, F. Residual stresses and mechanical properties of Si_3N_4/SiC multilayered composites with different SiC layers. *Bol. Soc. Esp. Ceram. Vidrio* **2017**, *56*, 147−154.
(12) Tien, C. L.; Lin, H. Y. Accurate prediction of multilayered residual stress in fabricating a mid-infrared long-wave pass filter with interfacial stress measurements. *Opt. Express* **2020**, *28*, 36994−37003.
(13) Li, B.; Fan, X.; Zhou, K.; Wang, T. A semi-analytical model for predicting stress evolution in multilayer coating systems during thermal cycling. *Int. J. Mech. Sci.* **2018**, *135*, 31−42.
(14) Tu, K. N.; Mayer, J. W.; Feldman, L. C. *Electronic Thin Film Science for Electrical Engineers and Materials Scientists: Solutions Manual*; Macmillan Publishing Company, 1992.
(15) Chason, E. A kinetic analysis of residual stress evolution in polycrystalline thin films. *Thin Solid Films* **2012**, *526*, 1−14.
(16) Korsunsky, A. M.; Salvati, E.; Lunt, A. G. J.; Sui, T.; Mughal, M. Z.; Daniel, R.; Keckes, J.; Bemporad, E.; Sebastiani, M. Nanoscale residual stress depth profiling by Focused Ion Beam milling and eigenstrain analysis. *Mater. Des.* **2018**, *145*, 55−64.
(17) Evans, A. G.; Hutchinson, J. W. The thermomechanical integrity of thin films and multilayers. *Acta Metall. Mater.* **1995**, *43*, 2507−2530.
(18) Wen, Y.; Basaran, C. Thermomechanical Stress Analysis of Multi-Layered Electronic Packaging. *J. Electron. Packag.* **2003**, *125*, 134−138.
(19) Suhir, E. Thermal Stress Failures in Electronics and Photonics: Physics, Modeling, Prevention. *J. Therm. Stresses* **2013**, *36*, 537−563.
(20) Hu, Y. Y.; Huang, W. M. Thermal Stress Analysis and Characterization of Thermomechanical Properties of Thin Films on

an Elastic Substrate. In *Handbook of Manufacturing Engineering and Technology*; Nee, A., Ed.; Springer, 2013; pp 1−71.
(21) Lassnig, A.; Putz, B.; Hirn, S.; Többens, D. M.; Mitterer, C.; Cordill, M. J. Adhesion evaluation of thin films to dielectrics in multilayer stacks: A comparison of four-point bending and stressed overlayer technique. *Mater. Des.* **2021**, *200*, No. 109451.
(22) Hsueh, C.-H. Modeling of elastic deformation of multilayers due to residual stresses and external bending. *J. Appl. Phys.* **2002**, *91*, 9652−9656.
(23) Hatte, Q.; Richard-Plouet, M.; Jouan, P.-Y.; Casari, P.; Dubos, P.-A. Simple and Versatile Analytical Method for Monitoring the Deposition of Thin Layers by Optical Measurement and Calculation of Residual Stress. *Thin Solid Films* **2021**, *725*, No. 138635.
(24) Hu, Y. Y.; Huang, W. M. Thermal Stress Analysis and Characterization of Themo-Mechanical Properties of Thin Films on an Elastic Substrate. In *Handbook of Manufacturing Engineering and Technology*; Nee, A. Y. C., Ed.; Springer, 2015; pp 3055−3133.
(25) Lee, S.; Kim, Y. Y.; Cho, Y. A Comparative Study on the Elastic Characteristics of an Aluminum Thin-Film Using Laser Optical Measurement Techniques. *Coatings* **2017**, *7*, 143.
(26) Sadek, K.; Moussa, W. Studying the Effect of Deposition Conditions on the Performance and Reliability of MEMS Gas Sensors. *Sensors* **2007**, *7*, 319−340.
(27) Kim, M. T. Influence of substrates on the elastic reaction of films for the microindentation tests. *Thin Solid Films* **1996**, *283*, 12−16.
(28) Tien, C. L.; Lin, T. W. Thermal expansion coefficient and thermomechanical properties of SiNx thin films prepared by plasma-enhanced chemical vapor deposition. *Appl. Opt.* **2012**, *51*, 7229−7235.
(29) Isono, Y.; Namazu, T.; Saito, Y.; Yamaguchi, A.; Fukushima, N. Effect of Gas Flow Ratio in PE-CVD on Elastic Properties of Sub-micron Thick Silicon Nitride Films for MEMS. In *Digest of Technical Papers, The 13th International Conference on Solid-State Sensors, Actuators and Microsystems (TRANSDUCERS '05)*, Seoul, Korea, June 5−9, 2005; Vol. *1*, pp 847−850.
(30) Pierson, H. O. 11 - Interstitial Nitrides: Properties and General Characteristics. In *Handbook of Refractory Carbides and Nitrides*; Pierson, H. O., Ed.; William Andrew Publishing, 1996; pp 181−208.
(31) Stone, D. S.; Yoder, K. B.; Sproul, W. D. Hardness and elastic modulus of TiN based on continuous indentation technique and new correlation. *J. Vac. Sci. Technol., A* **1991**, *9*, 2543−2547.
(32) Knibbs, R. H. The measurement of thermal expansion coefficient of tungsten at elevated temperatures. *J. Phys. E: Sci. Instrum.* **1969**, *2*, 515−517.
(33) Lassner, E.; Schubert, W.-D. The Element Tungsten. In *Tungsten: Properties, Chemistry, Technology of the Element, Alloys, and Chemical Compounds*; Lassner, E.; Schubert, W.-D., Eds.; Springer, 1999; pp 1−59.
(34) Timmie Topoleski, L. D.; Tsao, A. K.; Friis, E. A.; Jones, L. C. 3 - Fundamental principles of mechanical testing. In *Mechanical Testing of Orthopaedic Implants*; Friis, E., Ed.; Woodhead Publishing, 2017; pp 33−47.
(35) Ma, Y.; Hu, Z.; Tang, Y.; Sheng, Z.; Ma, S.; Hu, X.; Luo, W.; Zeng, Q.; Guo, L. Investigation of the mechanism and influence of laser wavelength and energy on laser opto-ultrasonic dual detection. *Appl. Opt.* **2020**, *59*, 9591−9597.
(36) Park, J.-W.; Lee, S.-H.; Yang, C.-W. Investigation of the interfacial adhesion of the transparent conductive oxide films to large-area flexible polymer substrates using laser-induced thermo-mechanical stresses. *J. Appl. Phys.* **2013**, *114*, No. 063513.
(37) Baba, T.; Taketoshi, N.; Yagi, T. Development of Ultrafast Laser Flash Methods for Measuring Thermophysical Properties of Thin Films and Boundary Thermal Resistances. *Jpn. J. Appl. Phys.* **2011**, *50*, No. 11RA01.
(38) Domanowski, P.; Betiuk, M. Recatest-A Technique for Qualitative and Quantitative Assessment of Deferment and Degraded PVD Coatings and CVD Layers in the Deformed Area in the Scratch Test. *Materials* **2021**, *14*, 2625.
(39) Zaman, S. B.; Hazrati, J.; de Rooij, M. B.; Matthews, D. T. A.; Venema, J.; van den Boogaard, A. H. Modeling crack initiation in Al-Si coating during heating/quenching phase of hot stamping process. In *11th Forming Technology Forum*, Zurich, Switzerland, 2018.
(40) Gupta, V.; Hernandez, R.; Wu, J.; Charconnet, P. Interfacial adhesion and its degradation in selected metal/oxide and dielectric/oxide interfaces in multi-layer devices. *Vacuum* **2000**, *59*, 292−300.
(41) Brinckmann, S.; Völker, B.; Dehm, G. Crack deflection in multi-layered four-point bending samples. *Int. J. Fract.* **2014**, *190*, 167−176.
(42) Freund, L. B.; Suresh, S. *Thin Film Materials: Stress, Defect Formation and Surface Evolution*; Cambridge University Press, 2004.
(43) Kim, G.; Lee, J.; Park, S.-h.; Kang, S.; Kim, T.-S.; Park, Y.-B. Comparison of Quantitative Interfacial Adhesion Energy Measurement Method between Copper RDL and WPR Dielectric Interface for FOWLP Applications. *J. Microelectron. Packag. Soc.* **2018**, *25*, 41−48.
(44) Völker, B.; Heinz, W.; Matoy, K.; Roth, R.; Batke, J. M.; Schöberl, T.; Scheu, C.; Dehm, G. Interface fracture and chemistry of a tungsten-based metallization on borophosphosilicate glass. *Philos. Mag.* **2015**, *95*, 1967−1981.
(45) Ma, Q. A four-point bending technique for studying subcritical crack growth in thin films and at interfaces. *J. Mater. Res.* **1997**, *12*, 840−845.
(46) Mahan, K.; Han, B. Four Point Bending Test for Adhesion Testing of Packaging Strictures: A Review. *J. Microelectron. Packag. Soc.* **2014**, *21*, 33−39.

https://doi.org/10.1021/acsomega.2c02122
ACS Omega 2022, 7, 25219−25228